Hadronic ZZ, W^-W^+, and $W^\pm Z$ production with QCD corrections and leptonic decays

J. Ohnemus
Department of Physics, University of California, Davis, California 95616
(Received 16 March 1994)

The processes $p\overset{(-)}{p} \to V_1V_2 + X \to \ell_1\bar{\ell}_1\ell_2\bar{\ell}_2 + X$, where $V_i = W^\pm$ or Z and ℓ_i denotes a lepton, are calculated to $O(\alpha_s)$. Total and differential cross sections, with acceptance cuts imposed on the final state leptons, are given for the Fermilab Tevatron and CERN LHC center of mass energies. Inclusive and exclusive 0-jet and 1-jet cross sections are given. The transverse momenta spectra of the leptons are significantly enhanced at high p_T by the QCD radiative corrections, especially at the LHC energy. Invariant mass and angular distributions are scaled up in magnitude by the QCD radiative corrections, but are little changed in shape.

PACS number(s): 13.85.Qk, 12.38.Bx, 14.70.Fm, 14.70.Hp

I. INTRODUCTION

The production of massive weak boson pairs (ZZ, W^-W^+, and $W^\pm Z$) is an important physics topic at high-energy hadron colliders. Measurements of these processes are vital for testing the standard model (SM) and probing beyond it. In particular, these processes are important for elucidating the electroweak symmetry-breaking mechanism and for testing the triple weak boson coupling [1]. Futhermore, these processes are also backgrounds to new physics signals, for example, new heavy particles such as neutral and charged Higgs bosons, technimesons, extra gauge bosons, squarks, and gluinos can all decay into weak boson pairs. It is therefore important to have precise calculations of hadronic weak boson pair production. These calculations should include the leptonic decays of the weak bosons since the weak bosons are identified via their leptonic decay products.

The dominant production mechanism for weak boson pairs in hadronic collisions is via the quark-antiquark annihilation subprocess $q_1\bar{q}_2 \to V_1V_2$. The cross sections for hadronic ZZ, W^-W^+, and $W^\pm Z$ production were first calculated in Refs. [2] and [3]. Tree level calculations of $V_1V_2 + n$ jets have been given for $n \leq 1$ and $n \leq 2$ in Refs. [4] and [5], respectively. ZZ and W^-W^+ can also be produced via the gluon fusion subprocess $gg \to VV$, which proceeds via a quark box loop and is of order α_s^2 [6–9]. The cross section for the gluon fusion process is significant at supercollider energies due to the large gluon luminosity, but it never dominates the $q\bar{q}$ annihilation cross section. Weak boson pairs can also be produced via the vector boson fusion process in which the incoming quarks radiate two vector bosons which subsequently scatter off each other [10]. This process is mainly of interest as a source of Higgs bosons, with the Higgs boson appearing as an s-channel resonance. Away from the Higgs boson peak, the weak-boson fusion production rate is only a small fraction of the basic $q_1\bar{q}_2 \to V_1V_2$ production rate. The QCD radiative corrections to hadronic ZZ [11,12], W^-W^+ [13,14], and $W^\pm Z$ [15,16] production have recently been calculated for the case of real weak bosons in the final state.

In this paper, previous calculations of next-to-leading-order (NLO) ZZ [11], W^-W^+ [13], and $W^\pm Z$ [15] production are extended to include the leptonic decays of the W and/or Z bosons. Since it is the decay products that are observed in an experiment, the inclusion of the leptonic decays in the calculation will make it much more useful for comparing with experimental data. Futhermore, cuts can now be applied to the final state leptons, thus allowing one to mimic the experimental conditions. The angular distributions of the weak boson's decay products are especially important because they are effective spin analyzers for the vector bosons [17]. They are also of crucial importance when one tries to distinguish the various sources of anomalous couplings in the three-boson vertex [17]. The NLO QCD corrections will have a significant effect on the distributions of the final state leptons, especially at the center-of-mass energy reached at the CERN Large Hadron Collider (LHC).

The calculations presented here include the leptonic decays of the weak bosons in the narrow width approximation. In this approximation, nonresonance diagrams (e.g., the final state $e\bar{e}\mu\bar{\mu}$, which is formed by the production and decay of ZZ, can also be reached by the process $pp \to Z \to e\bar{e}$ with the subsequent radiation of a leptonically decaying Z [$Z \to \mu\bar{\mu}$] from the electron line) are not necessary to maintain gauge invariance. The calculations are done by using the Monte Carlo method for NLO calculations [18] in combination with helicity amplitude methods [19]. The Monte Carlo method for NLO calculations is very powerful because any number of observables can be calculated simultaneously by simply histogramming the quantities of interest, experimental acceptance cuts can easily be imposed on the calculation, and it is also possible to compute the NLO QCD corrections for exclusive channels, e.g., $p\overset{(-)}{p} \to V_1V_2 + 0$ jet. Helicity amplitude methods make cross section calculations tractable for processes involving a large number of tree level diagrams; futhermore, the leptonic decays of the weak bosons are trivial to implement at the amplitude level.

The remainder of this paper is organized as follows. The formalism used in the calculations is described in Sec. II, numerical results for the Fermilab Tevatron and LHC center-of-mass energies are given in Sec. III, and summary remarks are given in Sec. IV. Technical details of the calculation have been relegated to an appendix.

II. FORMALISM

Next-to-leading-order calculations of hadronic ZZ, W^-W^+, and $W^\pm Z$ production have been presented for real weak bosons in the final state. These results are extended in this section to include the leptonic decays $W \to \ell\nu$ and $Z \to \ell\bar{\ell}$ ($\ell = e, \mu$). This section begins with a brief review of the NLO Monte Carlo formalism used in the calculation and concludes with a discussion of the incorporation of the leptonic decays.

The calculations are done using the narrow width approximation for the leptonically decaying weak bosons. This simplifies the calculation greatly for two reasons. First of all, it is possible to ignore the contributions from nonresonance Feynman diagrams without violating gauge invariance. An example of such a diagram is $q\bar{q} \to Z \to e\bar{e}$ followed by $\bar{e} \to \bar{e}Z \to \bar{e}\mu\bar{\mu}$, yielding the final state $e\bar{e}\mu\bar{\mu}$, which is the same final state produced by $q\bar{q} \to ZZ \to e\bar{e}\mu\bar{\mu}$. Second, in the narrow width approximation it is particularly easy to extend the NLO calculations of real weak boson pairs to include the leptonic decays of the W and Z bosons.

A. Monte Carlo formalism

The NLO calculations of V_1V_2 production include contributions from the square of the Born diagrams, the interference between the Born diagrams and the virtual one-loop diagrams, and the square of the real emission diagrams. (The Feynman diagrams for the case of real weak bosons in the final state can be found in the original references.) The calculations have been done using a combination of analytic and Monte Carlo integration methods [18]. The basic idea is to isolate the soft and collinear singularities associated with the real emission subprocesses by partitioning phase space into soft, collinear, and finite regions. This is done by introducing theoretical soft and collinear cutoff parameters, δ_s and δ_c. Using dimensional regularization [20], the soft and collinear singularities are exposed as poles in ϵ (the number of space-time dimensions is $N = 4 - 2\epsilon$ with ϵ a small number). The infrared singularities from the soft and virtual contributions are then explicitly canceled while the collinear singularities are factorized and absorbed into the definition of the parton distribution functions. The remaining contributions are finite and can be evaluated in four dimensions. The Monte Carlo program thus generates n-body (for the Born and virtual contributions) and $(n+1)$-body (for the real emission contributions) final state events. The n- and $(n+1)$-body contributions both depend on the cutoff parameters δ_s and δ_c, however, when these contributions are added together to form a suitably inclusive observable, all dependence on the cutoff parameters cancels. The numerical results presented in this paper are insensitive to variations of the cutoff parameters.

B. Summary of $O(\alpha_s)$ V_1V_2 production followed by leptonic decays

The formalism for $O(\alpha_s)$ hadronic weak boson pair production followed by leptonic decays of the weak bosons is summarized here. A detailed discussion about the incorporation of leptonic decays into a NLO calculation of a real weak boson pair can be found in Ref. [21], where the leptonic decay $W \to e\nu$ was incorporated into a NLO calculation of real $W\gamma$ production. Basically, except for the virtual contribution, all the NLO contributions for real V_1V_2 production have the form

$$d\sigma^{\rm NLO}(q_1\bar{q}_2 \to V_1V_2) = d\sigma^{\rm Born}(q_1\bar{q}_2 \to V_1V_2)\left[1 + C_F\frac{\alpha_s}{2\pi}(\cdots)\right], \quad (1)$$

where $\sigma^{\rm Born}$ is the lowest order Born contribution, $C_F = 4/3$ is the quark-gluon vertex color factor, and α_s is the strong running coupling. Thus the leptonic decays can be incorporated by simply making the replacement

$$d\sigma^{\rm Born}(q_1\bar{q}_2 \to V_1V_2) \longrightarrow d\sigma^{\rm Born}(q_1\bar{q}_2 \to V_1V_2 \to \ell_1\bar{\ell}_1\ell_2\bar{\ell}_2) \quad (2)$$

in the formulas for NLO real V_1V_2 production. The leptonic decays are particularly easy to incorporate when the calculation is done at the amplitude level; the weak-boson polarization vectors, $\epsilon_\mu(k)$, are simply replaced by the $V \to \ell\bar{\ell}$ decay currents, $J_\mu(k)$, in the amplitude. Details of the amplitude level calculations for the Born and real emission subprocesses can be found in Ref. [5].

The simple replacement described in the previous paragraph does not hold for the virtual corrections. Rather than undertake the nontrivial task of recalculating the virtual corrections for the case of leptonically decaying weak bosons, we have instead opted to use the virtual corrections for real on-shell weak bosons which we subsequently decay ignoring spin correlations. Neglecting spin correlations slightly modifies the shapes of the angular distributions of the final state leptons, but the total cross sections are not altered as long as no angular cuts (e.g., rapidity cuts) are imposed on the final state leptons. For realistic rapidity cuts, the total cross sections are changed by typically 10% when spin correlations are neglected. Since the virtual corrections are small (they are typically less than 10% as large as the corresponding

Born cross section) and the effects of spin correlations are small, the overall result of ignoring spin correlations in the virtual corrections is negligible compared to the 20%–30% uncertainty from the parton distribution functions and the choice of the scale Q^2. (Note that spin correlations are included everywhere in the calculations except in the virtual contributions.)

The results for the NLO calculation of $p\bar{p} \to V_1V_2 + X \to \ell_1\bar{\ell}_1\ell_2\bar{\ell}_2 + X$ can now be summarized. (The same formalism holds for pp collisions with the obvious replacement $\bar{p} \to p$.) The NLO cross section consists of four- and five-body final state contributions:

$$\sigma^{\rm NLO}(p\bar{p} \to V_1V_2 + X \to \ell_1\bar{\ell}_1\ell_2\bar{\ell}_2 + X) = \sigma^{\rm NLO}_{4\ \rm body}(p\bar{p} \to V_1V_2 \to \ell_1\bar{\ell}_1\ell_2\bar{\ell}_2) + \sigma_{5\ \rm body}(p\bar{p} \to V_1V_2 + X \to \ell_1\bar{\ell}_1\ell_2\bar{\ell}_2 + X)\,. \tag{3}$$

The four-body contribution is

$$\sigma^{\rm NLO}_{4\ \rm body}(p\bar{p} \to V_1V_2 \to \ell_1\bar{\ell}_1\ell_2\bar{\ell}_2) = \sigma^{\rm HC} + \sum_{q_1,\bar{q}_2}\int dv\,dx_1\,dx_2 \times\left[G_{q_1/p}(x_1,M^2)\,G_{\bar{q}_2/\bar{p}}(x_2,M^2)\,\frac{d\hat{\sigma}^{\rm NLO}}{dv}(q_1\bar{q}_2 \to V_1V_2 \to \ell_1\bar{\ell}_1\ell_2\bar{\ell}_2) + (x_1 \leftrightarrow x_2)\right], \tag{4}$$

where $\sigma^{\rm HC}$ is the contribution from the hard collinear remnants (see the Appendix for the definition), the sum is over all contributing quark flavors, v is related to the center-of-mass scattering angle θ^* by $v = \frac{1}{2}(1+\cos\theta^*)$, x_1 and x_2 are the parton momentum fractions, $G_{q/p}(x,M^2)$ is a parton distribution function, M^2 is the factorization scale, and

$$\begin{aligned}\frac{d\hat{\sigma}^{\rm NLO}}{dv}(q_1\bar{q}_2 \to V_1V_2 \to \ell_1\bar{\ell}_1\ell_2\bar{\ell}_2) = {}& \frac{d\hat{\sigma}^{\rm Born}}{dv}(q_1\bar{q}_2 \to V_1V_2 \to \ell_1\bar{\ell}_1\ell_2\bar{\ell}_2) \\ & \times\left[1 + C_F\frac{\alpha_s(\mu^2)}{2\pi}\left\{4\ln(\delta_s)^2 + 3\ln\left(\frac{\hat{s}}{M^2}\right) + 4\ln(\delta_s)\ln\left(\frac{\hat{s}}{M^2}\right)\right.\right. \\ & \left.\left. + \lambda_{\rm FC}\left[9 + \frac{2}{3}\pi^2 + 3\ln(\delta_s) - 2\ln(\delta_s)^2\right]\right\}\right] \\ & + \frac{d\hat{\sigma}^{\rm virt}}{dv}(q_1\bar{q}_2 \to V_1V_2)\,B(V_1 \to \ell_1\bar{\ell}_1)\,B(V_2 \to \ell_2\bar{\ell}_2)\,.\end{aligned} \tag{5}$$

The caret denotes a parton level cross section, $\alpha_s(\mu^2)$ is the strong running coupling evaluated at the renormalization scale μ^2, δ_s is the soft cutoff parameter, $\hat{s}$ is the square of the parton center-of-mass energy, and $\lambda_{\rm FC}$ specifies the factorization convention: $\lambda_{\rm FC} = 0$ for the universal [modified minimal subtraction ($\overline{\rm MS}$) [22]] convention and $\lambda_{\rm FC} = 1$ for the physical [deep inelastic scattering (DIS)] convention. The virtual contribution [23], $d\hat{\sigma}^{\rm virt}/dv(q_1\bar{q}_2 \to V_1V_2)$, is multiplied by the $V_1 \to \ell_1\bar{\ell}_1$ and $V_2 \to \ell_2\bar{\ell}_2$ branching ratios.

The five-body contribution is

$$\sigma_{5\ \rm body}(p\bar{p} \to V_1V_2 + X \to \ell_1\bar{\ell}_1\ell_2\bar{\ell}_2 + X) = \sum_{a,b,c}\int d\hat{\sigma}(ab \to V_1V_2c \to \ell_1\bar{\ell}_1\ell_2\bar{\ell}_2c) \times\left[G_{a/p}(x_1,M^2)\,G_{b/\bar{p}}(x_2,M^2) + (x_1 \leftrightarrow x_2)\right]dx_1\,dx_2\,, \tag{6}$$

where the sum is over all partons contributing to the three subprocesses $q_1\bar{q}_2 \to V_1V_2g \to \ell_1\bar{\ell}_1\ell_2\bar{\ell}_2g$, $q_1g \to V_1V_2q_2 \to \ell_1\bar{\ell}_1\ell_2\bar{\ell}_2q_2$, and $g\bar{q}_2 \to V_1V_2\bar{q}_1 \to \ell_1\bar{\ell}_1\ell_2\bar{\ell}_2\bar{q}_1$. The $2 \to 5$ subprocess is labeled by $p_1 + p_2 \to p_3 + p_4 + p_5 + p_6 + p_7$ and the kinematic invariants s_{ij} and t_{ij} are defined by $s_{ij} = (p_i + p_j)^2$ and $t_{ij} = (p_i - p_j)^2$. The integration over five-body phase space and $dx_1\,dx_2$ is done numerically by standard Monte Carlo techniques. The kinematic invariants s_{ij} and t_{ij} are first tested for soft and collinear singularities. If an invariant for a subprocess falls in a soft or collinear region of phase space, the contribution from that subprocess is not included in the cross section. The squared matrix elements for the Born and real emission subprocesses were evaluated numerically via helicity amplitude methods as described in Ref. [5]. No attempt has been made to antisymmetrize the amplitudes for the case of identical fermions in the final state.

III. PHENOMENOLOGICAL RESULTS

The phenomenological implications of NLO QCD corrections to V_1V_2 production at the Tevatron ($p\bar{p}$ collisions at $\sqrt{s} = 1.8$ TeV) and the LHC (pp collisions at $\sqrt{s} = 14$ TeV) will now be discussed. This section begins with a brief description of the input parameters and acceptance cuts.

A. Input parameters

The numerical results presented in this section were obtained using the two-loop expression for α_s. The QCD scale $\Lambda_{\rm QCD}$ is specified for four flavors of quarks by the choice of the parton distribution functions and is adjusted whenever a heavy-quark threshold is crossed so that α_s is a continuous function of Q^2. The heavy-quark masses were taken to be $m_b = 5$ GeV and $m_t = 150$ GeV. The SM parameters used in the numerical simulations are $M_Z = 91.173$ GeV, $M_W = 80.22$ GeV, $\alpha(M_W) = 1/128$, and $\sin^2\theta_{\rm w} = 1 - (M_W/M_Z)^2$. These values are consistent with recent measurements at the CERN e^+e^- collider LEP, the CERN $Sp\bar{p}S$ Collider, and the Fermilab Tevatron [24–26]. The soft and collinear cutoff parameters are fixed to $\delta_s = 10^{-2}$ and $\delta_c = 10^{-3}$ unless stated otherwise. The parton subprocesses have been summed over u, d, s, and c quarks, and the Cabibbo mixing angle has been chosen such that $\cos^2\theta_C = 0.95$. The leptonic branching ratios are $B(W \to e\nu) = 0.107$ and $B(Z \to e\bar{e}) = 0.034$, and the total widths of the W- and Z bosons are $\Gamma_W = 2.12$ GeV and $\Gamma_Z = 2.487$ GeV. A single scale $Q^2 = M^2_{V_1V_2}$, where $M_{V_1V_2}$ is the invariant mass of the V_1V_2 pair, has been used for the renormalization scale μ^2 and the factorization scale M^2.

In order to get consistent NLO results it is necessary to use parton distribution functions which have been fit to next-to-leading order. The numerical results were obtained using the the Martin-Roberts-Stirling (MRS) [27] set S0′ distributions with $\Lambda_4 = 215$ MeV. The MRS distributions are defined in the universal ($\overline{\rm MS}$) scheme, and thus the factorization defining parameter $\lambda_{\rm FC}$ in Eqs. (5) and (A2) should be $\lambda_{\rm FC} = 0$. For convenience, the MRS set S0′ distributions have also been used for the leading-order (LO) calculations.

B. Cuts

The cuts imposed in the numerical simulations are motivated by the finite acceptance and resolution of the detector. The finite acceptance of the detector is simulated by cuts on the four-vectors of the final state particles. These cuts include requirements on the transverse momentum p_T and pseudorapidity $\eta = \ln\cot(\theta/2)$ of the charged leptons and on the missing transverse momentum $\not{p}_T$ associated with the neutrino(s). Charged leptons are also required to be separated in azimuthal angle-pseudorapidity space, $\Delta R = [(\Delta\phi)^2 + (\Delta\eta)^2]^{1/2}$, where θ and ϕ are the polar and azimuthal angles relative to the beam; this cut is impelled by the finite granularity of the detector. The complete set of cuts can be summarized as follows:

Tevatron	LHC
$p_T(\ell) > 20$ GeV	$p_T(\ell) > 25$ GeV
$\not{p}_T > 20$ GeV	$\not{p}_T > 50$ GeV
$\lvert\eta(\ell)\rvert < 2.5$	$\lvert\eta(\ell)\rvert < 3.0$
$\Delta R(\ell,\ell) < 0.4$	$\Delta R(\ell,\ell) < 0.4$

C. NLO cross sections

The dependence of the total cross section on the soft and collinear cutoff parameters is illustrated in Fig. 1 which shows the total NLO cross section for $pp \to ZZ + X \to e^-e^+\mu^-\mu^+ + X$ plotted versus δ_s and δ_c, for $\sqrt{s} = 14$ TeV and the cuts described in Sec. III B.

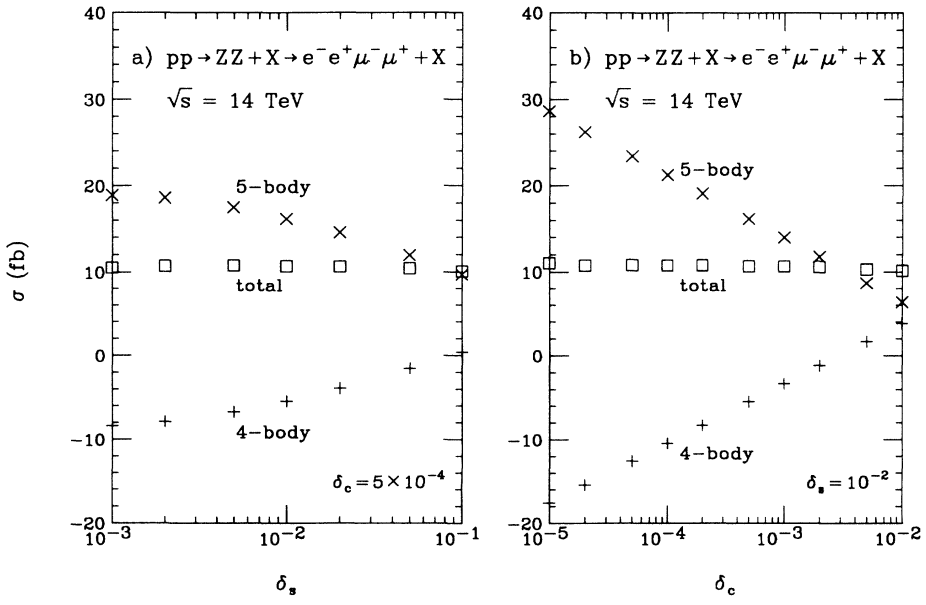

FIG. 1. The dependence of the total NLO cross section for $pp \to ZZ + X \to e^-e^+\mu^-\mu^+ + X$ at $\sqrt{s} = 14$ TeV on the soft and collinear cutoff parameters. In part (a) the total NLO cross section is plotted versus the soft cutoff parameter δ_s for a fixed value of $\delta_c = 5 \times 10^{-4}$. In part (b) the total NLO cross section is plotted versus the collinear cutoff parameter δ_c for a fixed value of $\delta_s = 10^{-2}$. The 4- and 5-body contributions are also shown. The cuts listed in Sec. III B have been imposed.

TABLE I. Total cross sections for $p\overset{(-)}{p} \to ZZ + X \to \ell_1\bar{\ell}_1\ell_2\bar{\ell}_2 + X$, $p\overset{(-)}{p} \to W^-W^+ + X \to \ell_1\bar{\nu}_1\nu_2\bar{\ell}_2 + X$, and $p\overset{(-)}{p} \to WZ + X \to \ell_1\nu_1\ell_2\bar{\ell}_2 + X$ for center-of-mass energies corresponding to the present Tevatron, an upgraded Tevatron, and the proposed LHC. The cross sections have been summed over $\ell = e, \mu$ and both charges of the W in the WZ process. The cuts listed in Sec. III B have been imposed.

$\sqrt{s}$ (TeV)	$p\overset{(-)}{p}$		$\sigma(ZZ)$ (fb)	$\sigma(W^-W^+)$ (fb)	$\sigma(W^\pm Z)$ (fb)
1.8	$p\bar{p}$	LO	4.8	190	17
		NLO	6.2	260	22
3.5	$p\bar{p}$	LO	12	440	44
		NLO	14	590	59
14	pp	LO	36	570	43
		NLO	43	960	77

The n- and $(n+1)$-body contributions are also plotted for illustration ($n = 4$ for this process). The figure shows that the 4- and 5-body contributions, which separately have no physical meaning, vary strongly with δ_s and δ_c, however, the total cross section, which is the sum of the 4- and 5-body contributions, is independent of δ_s and δ_c over a wide range of these parameters.

The total LO and NLO cross sections for weak-boson pair production, with the cuts specified in Sec. III B, are given in Table I for center-of-mass energies corresponding to the present Tevatron ($\sqrt{s} = 1.8$ TeV), an upgraded Tevatron ($\sqrt{s} = 3.5$ TeV), and the proposed LHC ($\sqrt{s} = 14$ TeV). The cross sections in Table I have been summed over $\ell = e, \mu$ and both charges of the W in the $W^\pm Z$ process.

For definiteness and convenience, differential cross sections will be given for the processes $p\overset{(-)}{p} \to ZZ + X \to e^-e^+\mu^-\mu^+ + X$, $p\overset{(-)}{p} \to W^-W^+ + X \to e^-\bar{\nu}_e\nu_e e^+ + X$, and $p\overset{(-)}{p} \to W^+Z + X \to \nu_e e^+\mu^-\mu^+ + X$. In practice, the final state leptons would be summed over $\ell = e, \mu$ and both charges of the W would be summed in the WZ process. Thus the distributions given here would be scaled up by the appropriate power of 2. The differential cross sections include the cuts described in Sec. III B. The figures are arranged in two parts, with parts (a) and (b) being the results for the Tevatron ($\sqrt{s} = 1.8$ TeV) and LHC ($\sqrt{s} = 14$ TeV) energies, respectively. Both NLO and LO results are shown. In some distributions, the NLO 0-jet exclusive and the LO 1-jet exclusive cross sections are also given. For these exclusive cross sections it is necessary to define a jet. A jet will be defined as a final state quark or gluon with

$$p_T(j) > 10 \text{ GeV} \quad \text{and} \quad |\eta(j)| < 2.5 \tag{7}$$

at the Tevatron, and

$$p_T(j) > 50 \text{ GeV} \quad \text{and} \quad |\eta(j)| < 3 \tag{8}$$

at the LHC. The sum of the NLO 0-jet and the LO 1-jet exclusive cross sections is equal to the inclusive NLO cross section.

D. ZZ production

The first process to be considered is $p\overset{(-)}{p} \to ZZ + X \to e^-e^+\mu^-\mu^+ + X$. The invariant mass distribution of the four leptons is displayed in Fig. 2; NLO and LO cross sections are shown. The NLO corrections are nearly uni-

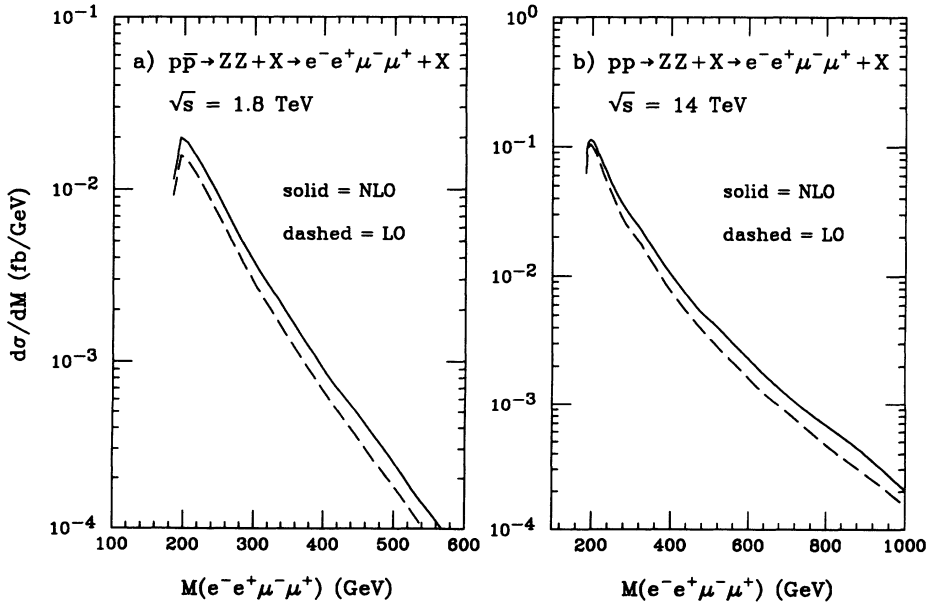

FIG. 2. The invariant mass of the four leptons in the process $p\overset{(-)}{p} \to ZZ + X \to e^-e^+\mu^-\mu^+ + X$. Parts (a) and (b) are for the Tevatron and LHC center-of-mass energies, respectively. The NLO (solid line) and LO (dashed line) cross sections are shown. The cuts listed in Sec. III B have been imposed.

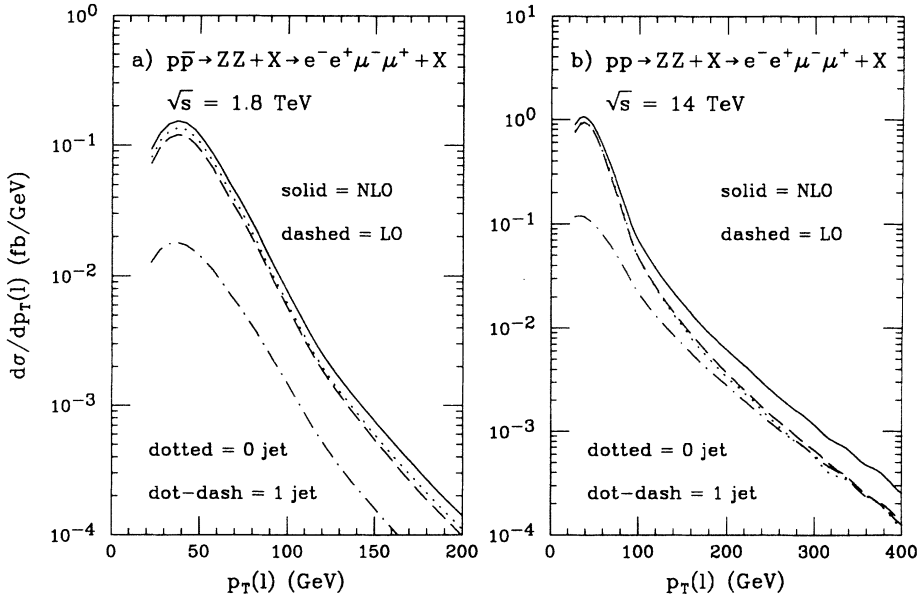

FIG. 3. Same as Fig. 2 but for the inclusive lepton transverse momentum distribution. The 0-jet (dotted line) and 1-jet (dot-dashed line) exclusive cross sections are also shown.

form in the invariant mass at the Tevatron energy and increase only slightly with the invariant mass at the LHC energy.

Figure 3 shows the inclusive differential cross section for the lepton transverse momentum (all four leptons have been histogrammed, each with the full event weight). At the Tevatron energy, the NLO corrections increase slowly with $p_T(\ell)$, whereas at the LHC energy, the corrections increase more rapidly with $p_T(\ell)$. The 0-jet and 1-jet exclusive cross sections are also shown. At the Tevatron energy, the 0-jet exclusive cross section is slightly larger than the LO cross section, while the 1-jet exclusive cross section is much smaller than the LO cross section. At the LHC energy, the 1-jet exclusive cross section is much smaller than the LO cross section at small values of $p_T(\ell)$, but becomes comparable to the LO cross section at large values of $p_T(\ell)$. The decomposition of the NLO cross section into 0-jet and 1-jet components shows that the large NLO corrections at high $p_T(\ell)$ are due to contributions from 1-jet real emission subprocesses. The 1-jet exclusive cross section becomes a larger fraction of the total NLO cross section at higher energies because the contributions from qg initial state processes grow with the center-of-mass energy due to the increasing gluon luminosity.

The 0-jet and 1-jet exclusive cross sections are, of course, arbitrary since they depend on the jet definition. For example, increasing the p_T threshold for a jet will suppress the 1-jet and enhance the 0-jet exclusive cross sections (the 0-jet and 1-jet exclusive cross sections must sum to the NLO cross section). Nevertheless, Fig. 3 illustrates that for reasonable jet definitions, the 1-jet contribution to the inclusive NLO cross section is small at the Tevatron energy, but becomes significant at the LHC energy, especially at high $p_T(\ell)$.

The inclusive differential cross section for the lepton pseudorapidity, $\eta = \ln\cot(\theta/2)$ where θ is the polar angle of the lepton with respect to the proton direction in the

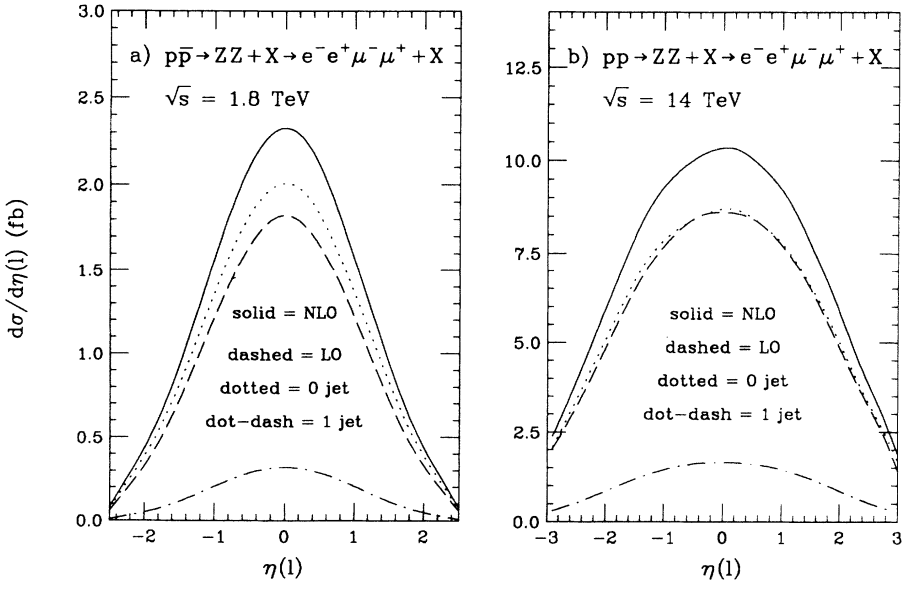

FIG. 4. Same as Fig. 2 but for the inclusive lepton pseudorapidity distribution.

laboratory frame, is given in Fig. 4. The NLO corrections are largest in the central rapidity region. The 0-jet and 1-jet exclusive cross sections are also shown. Notice that in the ZZ process, the 1-jet exclusive cross section is small compared to the NLO cross section. For the W^-W^+ and WZ processes, the 1-jet exclusive cross section becomes a larger fraction of the total NLO cross section.

The angular distributions of the leptonic decay products contain information on the helicities of the vector bosons. These distributions are simplest in the rest frame of the individual vector bosons. For the decay of a polarized Z-boson, $Z \to e^-e^+$, the angular distributions of the e^- in the Z-boson rest frame are

$$\frac{d\Gamma}{d\cos\theta}(\lambda_Z = 0) = \frac{G_F M_Z^3}{2\pi\sqrt{2}} (g_V^2 + g_A^2) \sin^2\theta , \quad (9)$$

$$\frac{d\Gamma}{d\cos\theta}(\lambda_Z = \pm 1) = \frac{G_F M_Z^3}{2\pi\sqrt{2}} \left[(g_V^2 + g_A^2) \tfrac{1}{2}(1 + \cos^2\theta) \pm 2 g_V g_A \cos\theta\right] , \quad (10)$$

where θ is the angle of the e^- with respect to the longitudinal axis and λ_Z denotes the polarization of the Z boson; $\lambda_Z = 0$ and $\lambda_z = \pm 1$ denote the longitudinal and transverse polarizations, respectively. Here G_F is the Fermi coupling constant and g_V (g_A) is the vector (axial vector) coupling of the Z boson to fermions. Since the Z-boson coupling to charged leptons is almost purely axial vector, transversely polarized Z bosons produce a $\frac{1}{2}(1 + \cos^2\theta)$ distribution for the e^-, while longitudinally polarized Z bosons yield a $\sin^2\theta$ distribution. Figure 5 shows the polar angle distribution of the e^- in the parent Z-boson rest frame, measured with respect to the parent Z boson direction in the ZZ rest frame, i.e., $\cos\theta_{e^-} = \hat{\mathbf{p}}_{e^-} \cdot \hat{\mathbf{p}}_Z$ where $\hat{\mathbf{p}}_{e^-}$ is the unit-normalized three-momentum of the e^- in the parent Z-boson rest frame and $\hat{\mathbf{p}}_Z$ is the unit-normalized three-momentum of the parent Z boson in the ZZ rest frame. The shapes of the distributions in Fig. 5 indicate that the transverse polarizations are dominating the cross section. This is to be expected since the $q\bar{q}$ annihilation process produces Z-boson pairs that are primarily transversely polarized, especially at large parton-center-of-mass energies. The sharp drops in the distributions near $\cos\theta_{e^-} = \pm 1$ are due to the kinematic cuts.

Figure 6 shows the angular correlation between the decay planes formed by the leptons. The angle χ between the decay planes is defined by

$$\cos\chi = \frac{(\mathbf{p}_{e^-} \times \mathbf{p}_{e^+}) \cdot (\mathbf{p}_{\mu^-} \times \mathbf{p}_{\mu^+})}{|\mathbf{p}_{e^-} \times \mathbf{p}_{e^+}| \; |\mathbf{p}_{\mu^-} \times \mathbf{p}_{\mu^+}|} , \quad (11)$$

where the momentum vectors are defined in the ZZ rest frame. The NLO and LO curves have the same shape at both energies. The shapes of these curves are dominated by the effects of the kinematic cuts; without cuts the curves are essentially flat [28].

E. W^-W^+ production

Attention now turns to the process $p\overset{(-)}{p} \to W^-W^+ + X \to e^-\bar{\nu}_e\nu_e e^+ + X$. Since there are two invisible neutrinos in the final state, much of the final state kinematic information is lost, and it is impossible to reconstruct the W^-W^+ invariant mass. The best one can do is form the transverse cluster mass [29] defined by

$$M_T^2(c, \not{p}_T) = \left[\sqrt{p_{cT}^2 + m_c^2} + |\not{p}_T|\right]^2 - \left[\mathbf{p}_{cT} + \not{\mathbf{p}}_T\right]^2 , \quad (12)$$

where c is either a single particle or a cluster of several particles. For the W^-W^+ process the cluster is $c = e^- + e^+$. The transverse cluster mass distribution is displayed

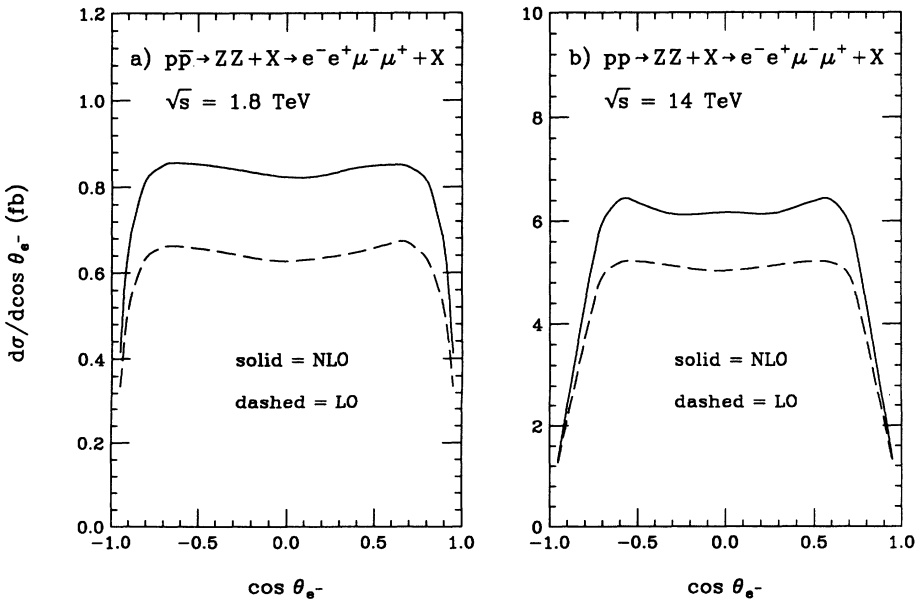

FIG. 5. Same as Fig. 2 but for the angular distribution of the e^-. The angle θ_{e^-} is measured in the parent Z-boson rest frame with respect to the parent Z-boson direction in the ZZ rest frame.

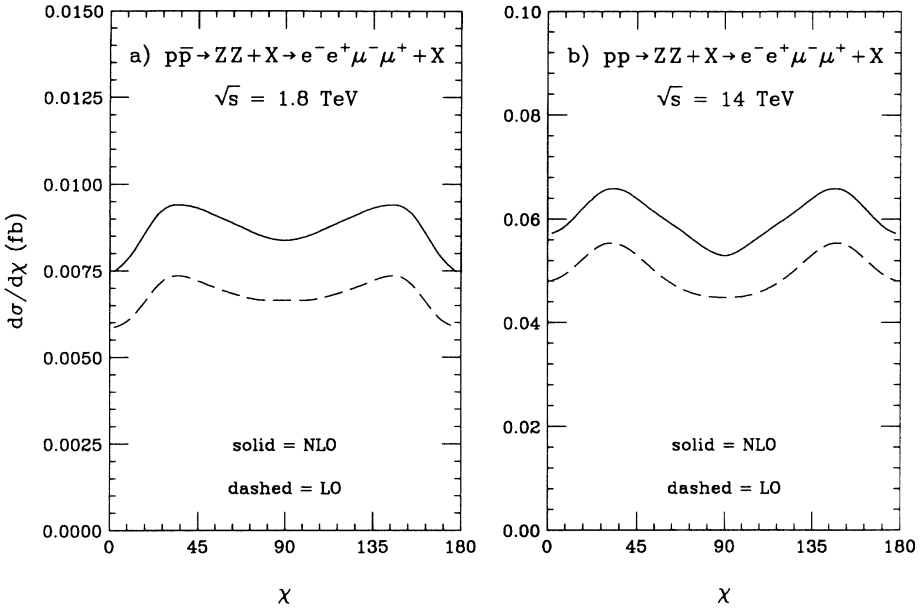

FIG. 6. Same as Fig. 2 but for the angular correlation between the lepton decay planes [see Eq. (11)].

in Fig. 7. The NLO corrections are nearly uniform in M_T at both the Tevatron and LHC energies. The invariant mass of the charged leptons, $M(e^-e^+)$, is also unchanged in shape by the NLO corrections.

Figure 8 shows the inclusive differential cross section for the charged lepton transverse momentum (both charged leptons have been histogrammed, each with the full event weight). The NLO corrections increase slowly with $p_T(\ell)$ at the Tevatron energy, but at the LHC energy, they increase very rapidly with $p_T(\ell)$. Similar behavior is observed in the p_T spectra of the W bosons [13,14]. The 0-jet and 1-jet exclusive cross sections are also shown. At the Tevatron energy, the 0-jet cross section is always larger than the 1-jet cross section. At the LHC energy, on the other hand, the 0-jet cross section dominates at small $p_T(\ell)$, while the 1-jet cross section dominates at high $p_T(\ell)$. This behavior is similar to that observed in the ZZ process, except now the 1-jet component is a larger fraction of the total NLO cross section.

The missing transverse momentum distribution is presented in Fig. 9. The $\not{p}_T$ distribution begins to fall rapidly when $\not{p}_T \approx M_W$. The NLO corrections increase with $\not{p}_T$ and become very large, especially at the LHC energy. The 0-jet and 1-jet cross sections are also shown. The 0-jet cross section dominates for $\not{p}_T \lesssim M_W$ while the 1-jet cross section dominates for $\not{p}_T > M_W$. The large NLO corrections at high $\not{p}_T$ are due to 1-jet events. At LO the W bosons are back to back in the transverse plane, thus when high p_T W bosons decay, the decay product neutrinos will also be nearly back to back in the transverse plane. The missing transverse momentum, which is the vector sum of the neutrino transverse momenta, thus

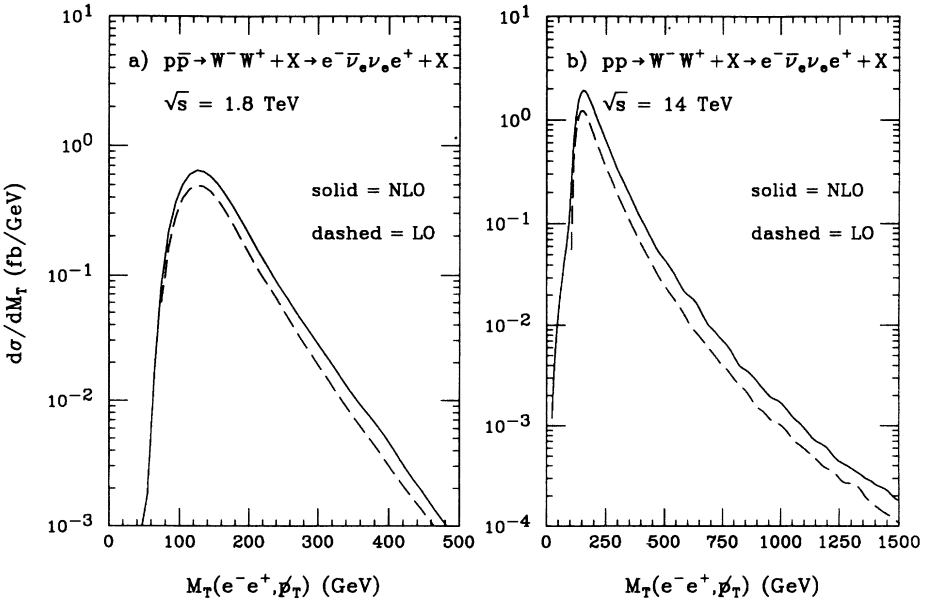

FIG. 7. The transverse cluster mass distribution for the process $pp \to W^-W^+ + X \to e^-\bar{\nu}_e\nu_e e^+ + X$. Parts (a) and (b) are for the Tevatron and LHC center-of-mass energies, respectively. The NLO (solid line) and LO (dashed line) cross sections are shown. The cuts listed in Sec. III B have been imposed.

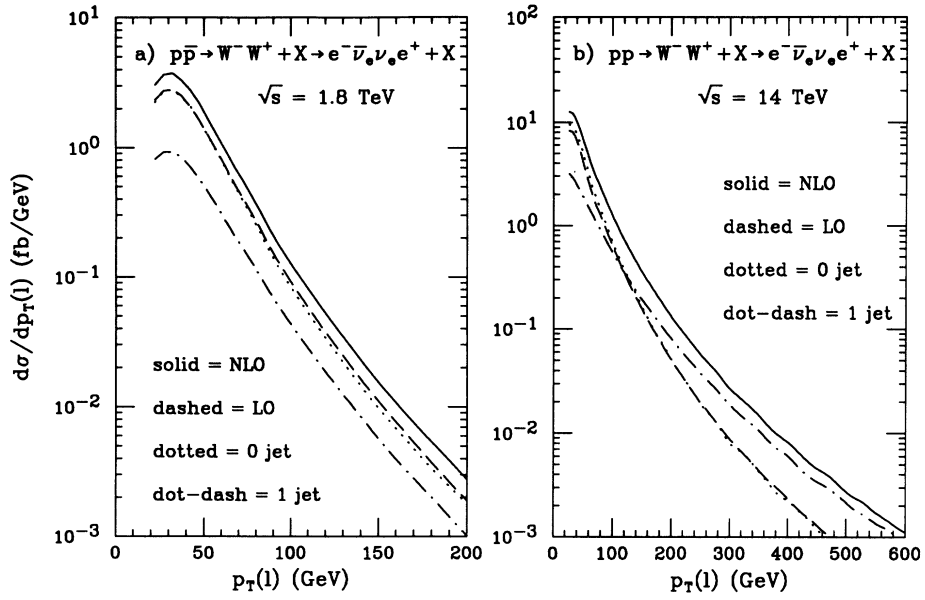

FIG. 8. Same as Fig. 7 but for the inclusive charged lepton transverse momentum distribution. The 0-jet (dotted line) and 1-jet (dot-dashed line) exclusive cross sections are also shown.

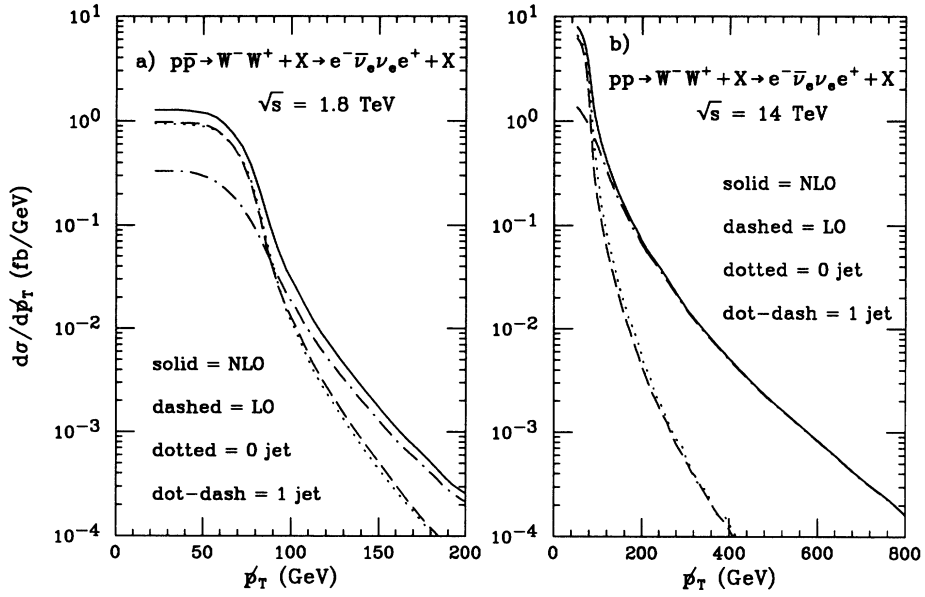

FIG. 9. Same as Fig. 7 but for the missing transverse momentum distribution.

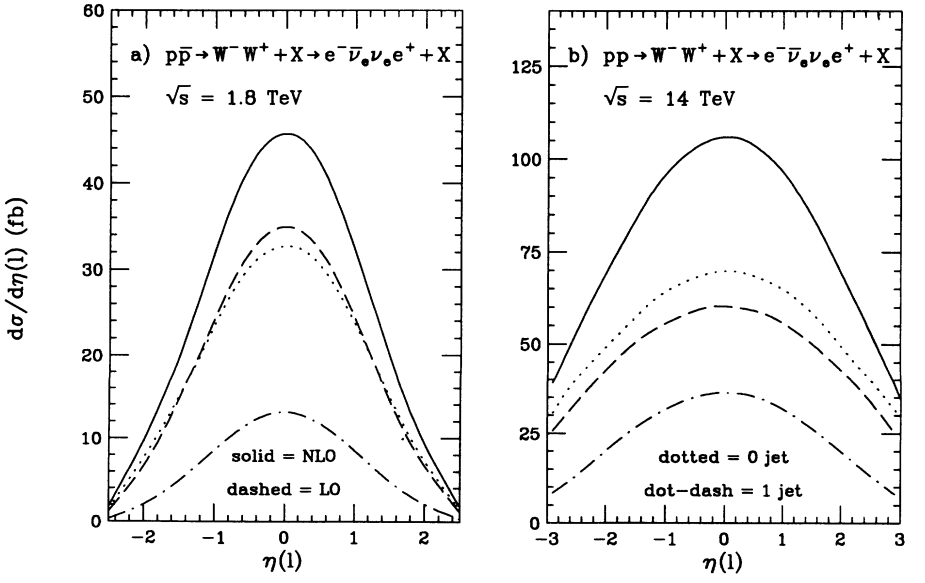

FIG. 10. Same as Fig. 7 but for the inclusive charged lepton pseudorapidity distribution.

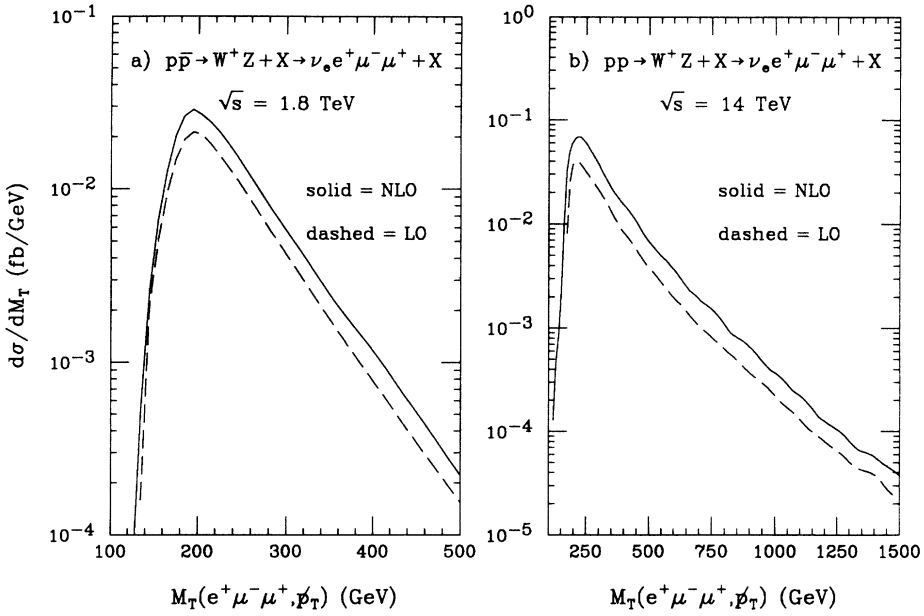

FIG. 11. The transverse cluster mass distribution for the process $p\overset{(-)}{p} \to W^+Z + X \to \nu_e e^+\mu^-\mu^+ + X$. Parts (a) and (b) are for the Tevatron and LHC center-of-mass energies, respectively. The NLO (solid line) and LO (dashed line) cross sections are shown. The cuts listed in Sec. III B have been imposed.

tends to be small due to the acollinear cancellation of the neutrino momenta and the $\not{p}_T$ distribution falls rapidly. On the other hand, when a W^-W^+ event contains a high p_T jet, the transverse angle between the decay product neutrinos can easily be acute, thus yielding a much larger value of $\not{p}_T$.

Figure 10 shows the inclusive pseudorapidity distribution of the charged leptons. The NLO corrections are once again largest in the central pseudorapidity region. The 0-jet and 1-jet exclusive cross sections are also shown. The interesting feature to note is that compared to the corresponding distribution for the ZZ process (Fig. 4), the 1-jet cross section for the W^-W^+ process is a larger fraction of the total NLO cross section. This trend will continue for the WZ process.

F. WZ production

The final process to be considered is $p\overset{(-)}{p} \to W^+Z + X \to \nu_e e^+\mu^-\mu^+ + X$. This process is of special interest because it is sensitive to the WWZ vertex. The discussion here will be limited to the case of standard model couplings at the WWZ vertex. A study of this process with NLO corrections and anomalous couplings at the WWZ vertex can be found in Ref. [30].

The transverse cluster mass [see Eq. (12)], where the cluster is $c = e^+ + \mu^- + \mu^+$, is shown in Fig. 11. The NLO corrections are nearly uniform in M_T at both the Tevatron and LHC energies. Since there is only one neutrino in the final state, it is possible to reconstruct the

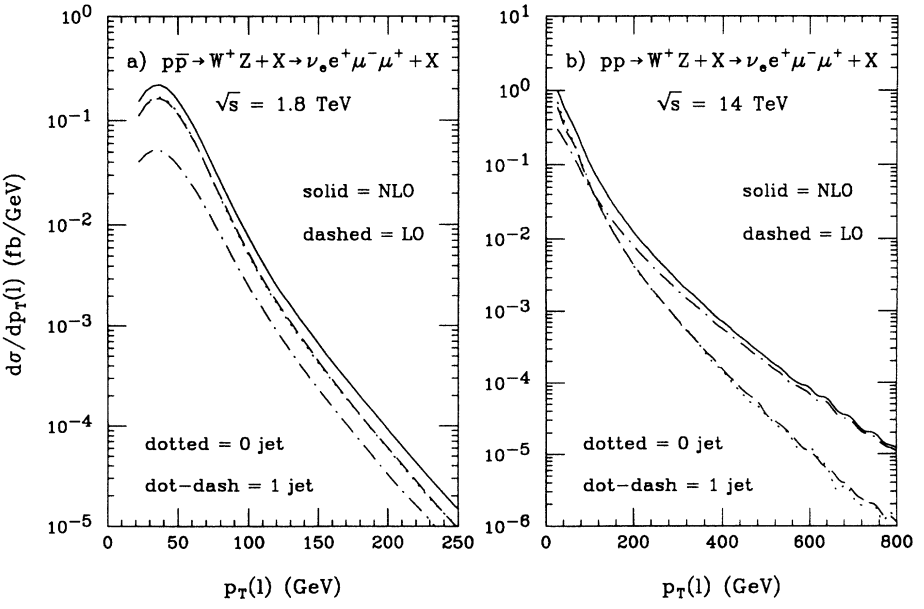

FIG. 12. Same as Fig. 11 but for the inclusive charged lepton transverse momentum distribution. The 0-jet (dotted line) and 1-jet (dot-dashed line) exclusive cross sections are also shown.

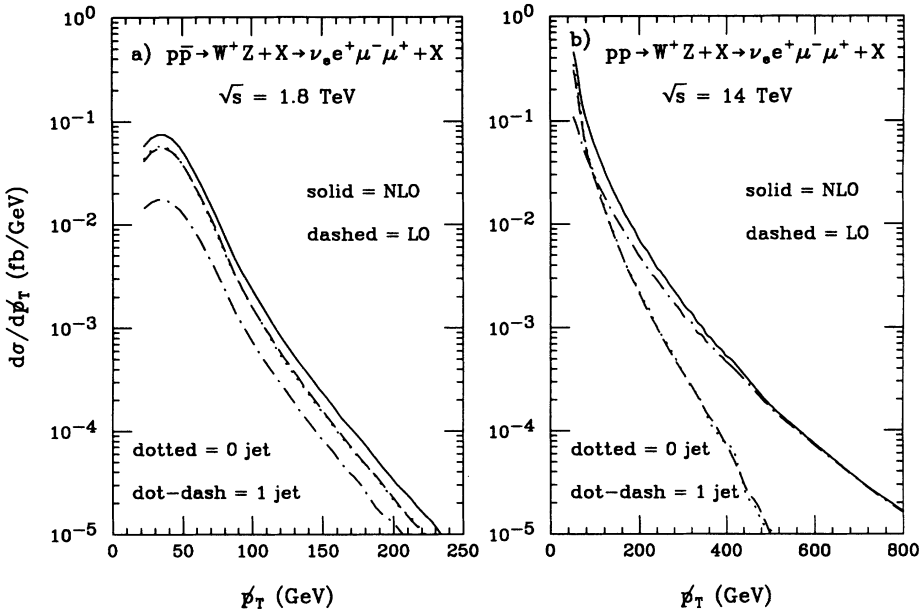

FIG. 13. Same as Fig. 11 but for the missing transverse momentum distribution.

WZ invariant mass by requiring the invariant mass of the electron plus neutrino system to be equal to the W-boson mass. This constraint gives a quadratic solution for the longitudinal momentum of the neutrino, and thus there is a two-fold ambiguity in the reconstructed WZ invariant mass. The reconstructed WZ invariant mass, formed by histogramming both reconstructed invariant masses, each with half the event weight, is qualitatively similar to the cluster transverse mass. In particular, the shape of the reconstructed WZ invariant mass is unchanged by the NLO corrections.

Figure 12 shows the inclusive transverse momentum distribution of the charged leptons (all three charged leptons have been histogrammed, each with the full event weight). The NLO corrections once again increase with $p_T(\ell)$ and are especially large at the LHC energy. The 0-jet exclusive cross section is the dominant component of the inclusive NLO cross section at the Tevatron energy, whereas at the LHC, the 0-jet cross section dominates at small $p_T(\ell)$ while the 1-jet cross section dominates at high $p_T(\ell)$. The $\not{p}_T$ distribution, which is shown in Fig. 13, exhibits the same qualitative features as the $p_T(\ell)$ distribution.

The inclusive pseudorapidity distribution of the charged leptons is displayed in Fig. 14. Note that the 1-jet cross section is now an even larger fraction of the total NLO cross section than it was in either the ZZ or W^-W^+ process (see Figs. 4 and 10).

Figure 15 shows the polar angle distribution of the e^+ in the W-boson rest frame, measured with respect to the W-boson direction in the W^+Z rest frame, i.e., $\cos\theta_{e^+} = \hat{\mathbf{p}}_{e^+} \cdot \hat{\mathbf{p}}_W$ where $\hat{\mathbf{p}}_{e^+}$ is the unit-normalized three-momentum of the e^+ in the W-boson rest frame and $\hat{\mathbf{p}}_W$ is the unit-normalized three-momentum of the

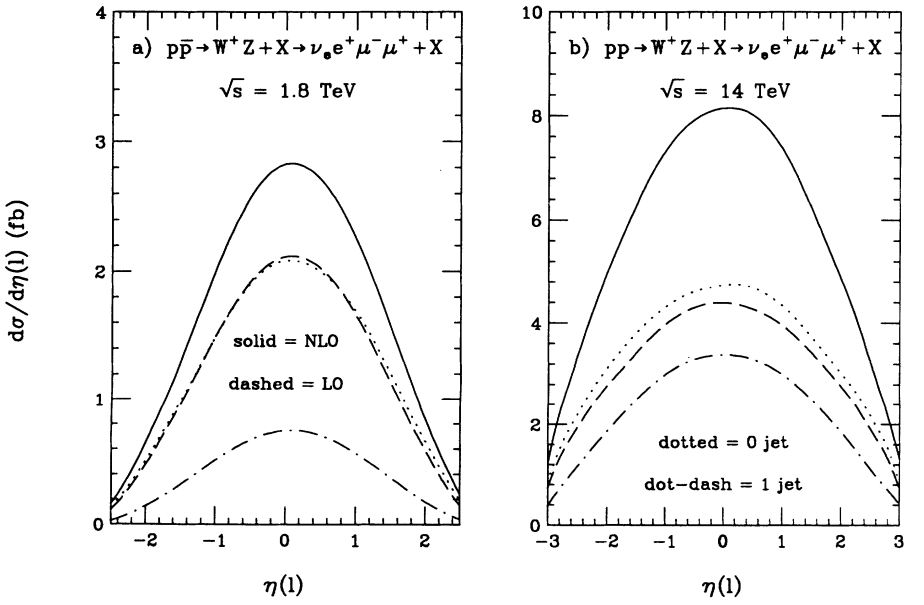

FIG. 14. Same as Fig. 11 but for the inclusive charged lepton pseudorapidity distribution.

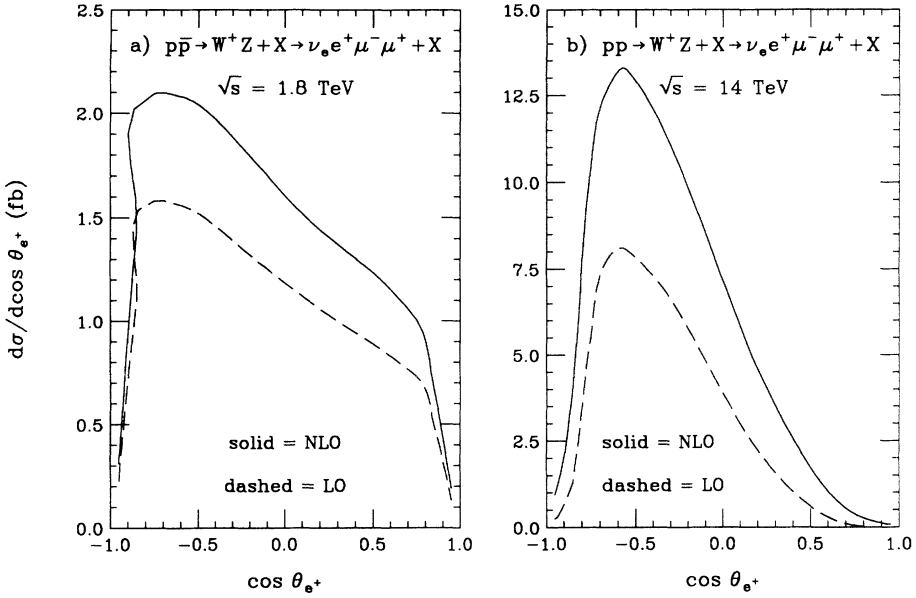

FIG. 15. Same as Fig. 11 but for the angular distribution of the e^+. The angle θ_{e^+} is measured in the W-boson rest frame with respect to the W-boson direction in the WZ rest frame.

W boson in the WZ rest frame. The $\cos\theta_{e+}$ distribution, and the analogous $\cos\theta_{\mu^-}$ distribution discussed in the next paragraph, both contain twofold ambiguities corresponding to the two solutions for the longitudinal momentum of the neutrino. Both solutions have been histogrammed, each with half the event weight. For the decay of a polarized W boson, $W^+ \to e^+\nu_e$, the angular distributions of the e^+ in the W-boson rest frame are

$$\frac{d\Gamma}{d\cos\theta}(\lambda_W = 0) = \frac{G_F M_W^3}{8\pi\sqrt{2}} \sin^2\theta\,, \tag{13}$$

$$\frac{d\Gamma}{d\cos\theta}(\lambda_W = \pm 1) = \frac{G_F M_W^3}{8\pi\sqrt{2}} \frac{1}{2}(1 \pm \cos\theta)^2\,, \tag{14}$$

where θ is the angle of the e^+ with respect to the longitudinal axis and $\lambda_W = 0$ (± 1) denotes the longitudinal (transverse) polarization(s) of the W^+ boson. The $q\bar{q}$ annihilation process produces WZ pairs that are primarily transversely polarized, furthermore, for $q_1\bar{q}_2 \to W^+Z$, the helicity combination ($\lambda_W = -1, \lambda_Z = 1$) gives the dominant contribution [31]. This explains the $\frac{1}{2}(1-\cos\theta)^2$ shape of the $\cos\theta_{e+}$ distribution in Fig. 15. The distributions fall near $\cos\theta_{e+} = \pm 1$ due to the kinematic cuts.

Figure 16 shows the polar angle distribution of the μ^- in the Z-boson rest frame, measured with respect to the Z-boson direction in the W^+Z rest frame, i.e., $\cos\theta_{\mu^-} = \hat{\mathbf{p}}_{\mu^-} \cdot \hat{\mathbf{p}}_Z$ where $\hat{\mathbf{p}}_{\mu^-}$ is the unit-normalized three-momentum of the μ^- in the Z-boson rest frame and $\hat{\mathbf{p}}_Z$ is the unit-normalized three-momentum of the Z boson in the WZ rest frame. Vestiges of the $\frac{1}{2}(1+\cos^2\theta)$ distribution characteristic of transversely polarized Z bosons can be seen in the figure. The asymmetry in the distributions comes from the $\cos\theta$ term in Eq. (10) and has a negative slope because the dominant contribution comes from the helicity combination ($\lambda_W = -1, \lambda_Z = 1$).

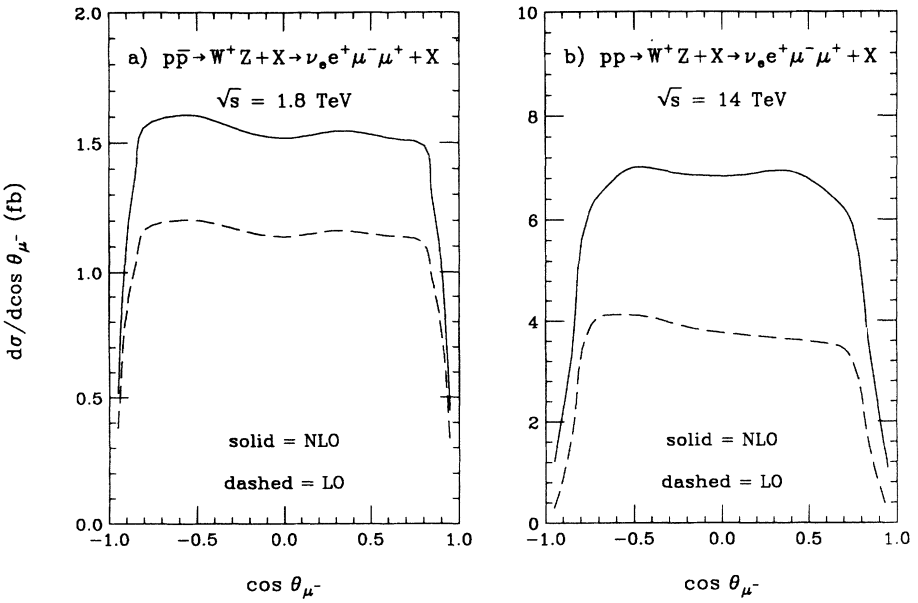

FIG. 16. Same as Fig. 11 but for the angular distribution of the μ^-. The angle θ_{μ^-} is measured in the Z-boson rest frame with respect to the Z-boson direction in the WZ rest frame.

G. Discussion

Comparing the three processes, one sees that the NLO corrections increase for the processes in the order ZZ, W^-W^+, WZ. The 1-jet exclusive cross section also becomes a larger fraction of the total NLO cross section in this same order. Both of these features are due to the $qg \to V_1V_2q$ real emission subprocesses.

A decomposition of the NLO corrections into components from order α_s $q\bar{q}$ and qg initial states shows that the $q\bar{q}$ components are of similar size in all three processes (the $q\bar{q}$ component is approximately 10% the size of the corresponding Born cross section), whereas the order α_s qg component increases for the processes in the order ZZ, W^-W^+, WZ [15,16,14]. A similar decomposition of the 1-jet exclusive cross section exhibits the same behavior.

The NLO corrections and the 1-jet fraction are largest for the WZ process because the Born cross section for this process is suppressed due to destructive interference between the S-, T-, and U-channel Feynman diagrams. This destructive interference produces an approximate amplitude zero [31]; the dominant helicity amplitudes ($\lambda_W = \pm 1, \lambda_Z = \mp 1$) have an exact zero, whereas the other helicity amplitudes remain finite but small. The situation is analogous to the $q\bar{q} \to W\gamma$ process which, because of the massless photon, has an exact zero in all the helicity amplitudes [32]. The NLO QCD corrections to the process $q\bar{q} \to W\gamma$ are very large at high center-of-mass energies as a result of the destructive interference and the large gluon luminosity [33]. The approximate amplitude zero in the $q\bar{q} \to WZ$ process produces dips in the distributions of $\cos\theta^*$ [31], y_Z^*, and $y_Z - y_W$ [16], where θ^* is the center-of-mass scattering angle, y_Z^* is the Z-boson rapidity in the WZ center of mass frame, and y_Z (y_W) is the Z-boson (W-boson) rapidity in the laboratory frame. The approximate amplitude zero also suppresses the WZ Born cross section at high $p_T(Z)$. The $qg \to WZq$ subprocess, on the other hand, is not suppressed by destructive interference. As a result, the NLO corrections and the 1-jet fraction are larger for the WZ process than for either the ZZ or W^-W^+ process.

In all three processes, the NLO corrections are largest at high p_T because the $qg \to V_1V_2q$ subprocesses are enhanced in diagrams where a weak boson and a quark are produced at high p_T, with the quark radiating the other weak boson, i.e., diagrams in which $qg \to V_1q$ followed by $q \to qV_2$. These subprocesses are enhanced by a factor $\ln^2(p_T(V_1)/M_{V_2})$ [16,14], which arises from the kinematic region where V_2 is nearly collinear to the quark.

The W^-W^+ process has a larger NLO correction and a larger 1-jet fraction than the ZZ process. These features are again due to differences in the relative importance of the qg initial state processes. The qg initial state processes are of more relative importance for the W^-W^+ process than for the ZZ process; however, it is not clear why this is so. The mass difference between the W and Z boson is not enough to explain the difference.

Another notable feature of the NLO corrections is that they increase with the center-of-mass energy. This behavior is also due to the qg initial state processes. The contributions from these processes increases with the center-of-mass energy due to the increasing the gluon luminosity.

IV. SUMMARY

The QCD radiative corrections to hadronic ZZ, W^-W^+, and $W^\pm Z$ production have been calculated to order α_s with leptonic decays of the weak bosons included. The inclusion of the leptonic decays makes the calculations more realistic since it is the leptonic decay products that are observed in an experiment. Distributions of the final state decay products have been given for both inclusive and exclusive channels for the Tevatron and LHC center-of-mass energies. The calculations include typical acceptance cuts on the final state leptons.

The calculations were done by using the Monte Carlo method for NLO calculations in combination with helicity amplitude methods. With the Monte Carlo method it is easy to impose experimentally motivated acceptance cuts on the final state leptons, also, it is possible to calculate the order α_s QCD corrections for exclusive channels, e.g., $p\overset{(-)}{p} \to V_1V_2 + 0$ jet. The narrow width approximation has been used for the decaying weak bosons. This simplifies the calculation greatly since it is possible to ignore contributions from nonresonant Feynman diagrams without violating gauge invariance. Futhermore, in the narrow width approximation it is particularly easy to extend previous NLO calculations of real weak boson pairs to include the leptonic decays of the weak bosons. Spin correlations are included everywhere in the calculation except in the virtual contributions where they can be safely neglected. Nevertheless, it would be desirable to include spin correlations in the virtual contributions in the future.

The QCD radiative corrections enhance the transverse momenta spectra of the leptons at high p_T, especially at the LHC energy. These enhancements are due to the opening of the qg subprocesses at order α_s. The contribution from these processes increases with the center-of-mass energy due to the increasing gluon density in the proton. Invariant mass and angular distributions are scaled up in magnitude by the QCD radiative corrections, but undergo little change in shape.

ACKNOWLEDGMENTS

The author would like to thank U. Baur, J. F. Gunion, T. Han, and D. Zeppenfeld for useful discussions. This work has been supported in part by Department of Energy Grant No. DE-FG03-91ER40674 and by Texas National Research Laboratory Grant No. RGFY93-330.

APPENDIX: HARD COLLINEAR CORRECTIONS

The real emission subprocesses $q_1(p_1) + \bar{q}_2(p_2) \to V_1V_2g \to \ell_1(p_3) + \bar{\ell}_1(p_4) + \ell_2(p_5) + \bar{\ell}_2(p_6) + g(p_7)$ (and the cross subprocesses) have hard collinear singularities when $t_{17} \to 0$ or $t_{27} \to 0$ [$t_{ij} = (p_i - p_j)^2$]. These singularities must be factorized and absorbed into the initial state parton distribution functions. After the factorization is performed, the contribution from the remnants of the hard collinear singularities has the form

$$\sigma^{\rm HC} = \sum_{q_1,\bar{q}_2} \int \frac{\alpha_s}{2\pi} \frac{d\hat{\sigma}^{\rm Born}}{dv}(q_1\bar{q}_2 \to V_1V_2 \to \ell_1\bar{\ell}_1\ell_2\bar{\ell}_2)\, dv\, dx_1\, dx_2 \Bigg[G_{q_1/p}(x_1,M^2) \int_{x_2}^{1-\delta_s} \frac{dz}{z} G_{\bar{q}_2/\bar{p}}\Big(\frac{x_2}{z},M^2\Big)\tilde{P}_{qq}(z)$$
$$+G_{q_1/p}(x_1,M^2)\int_{x_2}^{1}\frac{dz}{z}G_{g/\bar{p}}\Big(\frac{x_2}{z},M^2\Big)\tilde{P}_{qg}(z)+G_{\bar{q}_2/\bar{p}}(x_2,M^2)\int_{x_1}^{1-\delta_s}\frac{dz}{z}G_{q_1/p}\Big(\frac{x_1}{z},M^2\Big)\tilde{P}_{qq}(z)$$
$$+G_{\bar{q}_2/\bar{p}}(x_2,M^2)\int_{x_1}^{1}\frac{dz}{z}G_{g/p}\Big(\frac{x_1}{z},M^2\Big)\tilde{P}_{qg}(z)\Bigg], \tag{A1}$$

with

$$\tilde{P}_{ij}(z) \equiv P_{ij}(z)\ln\Big(\frac{1-z}{z}\delta_c\frac{s_{12}}{M^2}\Big) - P'_{ij}(z) - \lambda_{\rm FC}F_{ij}(z)\,. \tag{A2}$$

The Altarelli-Parisi splitting functions in $N = 4 - 2\epsilon$ dimensions for $0 < z < 1$ are

$$P_{qq}(z,\epsilon) = C_F\left[\frac{1+z^2}{1-z} - \epsilon(1-z)\right], \tag{A3}$$

$$P_{qg}(z,\epsilon) = \frac{1}{2(1-\epsilon)}\left[z^2+(1-z)^2-\epsilon\right], \tag{A4}$$

and can be written as

$$P_{ij}(z,\epsilon) = P_{ij}(z) + \epsilon P'_{ij}(z)\,, \tag{A5}$$

which defines the P'_{ij} functions. The functions F_{qq} and F_{qg} depend on the choice of factorization convention and the parameter $\lambda_{\rm FC}$ specifies the factorization convention; $\lambda_{\rm FC} = 0$ for the universal [modified minimal subtraction ($\overline{\rm MS}$) [22]] convention and $\lambda_{\rm FC} = 1$ for the physical [deep inelastic scattering (DIS)] convention. For the physical convention the factorization functions are

$$F_{qq}(z) = C_F\left[\frac{1+z^2}{1-z}\ln\Big(\frac{1-z}{z}\Big) - \frac{3}{2}\frac{1}{1-z} + 2z + 3\right], \tag{A6}$$

$$F_{qg}(z) = \frac{1}{2}\Big[\{z^2+(1-z)^2\}\ln\Big(\frac{1-z}{z}\Big) + 8z(1-z) - 1\Big]. \tag{A7}$$

The transformation between the $\overline{\rm MS}$ and DIS schemes is discussed in Ref. [34]. The parameter M^2 is the factorization scale which must be specified in the process of factorizing the collinear singularity. Basically, it determines how much of the collinear term is absorbed into the various parton distribution functions.

[1] E. Eichten, I. Hinchliffe, K. Lane, and C. Quigg, Rev. Mod. Phys. **56**, 579 (1984); **58**, 1065(E) (1986).

[2] R. W. Brown and K. O. Mikaelian, Phys. Rev. D **19**, 922 (1979).

[3] R. W. Brown, K. O. Mikaelian, and D. Sahdev, Phys. Rev. D **20**, 1164 (1979).

[4] U. Baur, E. W. N. Glover, and J. J. van der Bij, Nucl. Phys. **B318**, 106 (1989).

[5] V. Barger, T. Han, J. Ohnemus, and D. Zeppenfeld, Phys. Rev. D **41**, 2782 (1990).

[6] J. C. Pumplin, W. W. Repko, and G. L. Kane, in *Physics of the Superconducting Super Collider, Snowmass, 1986*, Proceedings of the Summer Study, Snowmass, Colorado, edited by R. Donaldson and J. Marx (Division of Particles and Fields of the APS, New York, 1987); D. A. Dicus, C. Kao, and W. W. Repko, Phys. Rev. D **36**, 1570 (1987); D. A. Dicus, *ibid.* **38**, 394 (1988).

[7] E. W. N. Glover and J. J. van der Bij, Phys. Lett. B **219**, 488 (1989); Nucl. Phys. **B321**, 561 (1989).

[8] D. A. Dicus and C. Kao, Phys. Rev. D **43**, 1555 (1991); E. W. N. Glover and J. J. van der Bij, Phys. Lett. B **219**, 488 (1989).

[9] H. Georgi, S. L. Glashow, M. E. Machacek, and D. V. Nanopoulos, Phys. Rev. Lett. **40**, 692 (1978).

[10] M. J. Duncan, G. L. Kane, and W. W. Repko, Nucl. Phys. **B272**, 517 (1986); M. J. Duncan, Phys. Lett. B **179**, 393 (1986); A. Abbasabadi and W. W. Repko, *ibid.* **199**, 286 (1986); R. Kleiss and W. J. Stirling, *ibid.* **182**, 75 (1986); J. F. Gunion, J. Kalinowski, and A. Tofighi-Niaki, Phys. Rev. Lett. **57**, 2351 (1986); D. A. Dicus, S. L. Wilson, and R. Vega, Phys. Lett. B **192**, 231 (1987); A. Abbasabadi and W. W. Repko, Nucl. Phys. **B292**, 461 (1987); Phys. Rev. D **36**, 289 (1987); **37**, 2668 (1988); D. A. Dicus and R. Vega, *ibid.* **37**, 2474 (1988); Phys. Rev. Lett. **57**, 1110 (1986).

[11] J. Ohnemus and J. F. Owens, Phys. Rev. D **43**, 3626 (1991).

[12] B. Mele, P. Nason, and G. Ridolfi, Nucl. Phys. **B357**, 409 (1991).

[13] J. Ohnemus, Phys. Rev. D **44**, 1403 (1991).

[14] S. Frixione, Nucl. Phys. **B410**, 280 (1993).

[15] J. Ohnemus, Phys. Rev. D **44**, 3477 (1991).

[16] S. Frixione, P. Nason, and G. Ridolfi, Nucl. Phys. **B383**, 3 (1992).

[17] S. Willenbrock and D. Zeppenfeld, Phys. Rev. D **37**, 1775 (1988).

[18] H. Baer, J. Ohnemus, and J. F. Owens, Phys. Rev. D **40**, 2844 (1989); **42**, 61 (1990); Phys. Lett. B **234**, 127 (1990); H. Baer and M. H. Reno, Phys. Rev. D **43**, 2892 (1991); B. Bailey, J. Ohnemus, and J. F. Owens, *ibid.*

46, 2018 (1992); J. Ohnemus and W. J. Stirling, *ibid.* **47**, 2722 (1993); H. Baer, B. Bailey, and J. F. Owens, *ibid.* **47**, 2730 (1993); L. Bergmann, Ph.D. dissertation, Florida State University, Report No. FSU-HEP-890215, 1989 (unpublished).

[19] P. De Causmaecker, R. Gastmans, W. Troost, and T. T. Wu, Phys. Lett. **105B**, 215 (1981); Nucl. Phys. **B206**, 53 (1982); F. A. Berends, R. Kleiss, P. De Causmaecker, R. Gastmans, W. Troost, and T. T. Wu, *ibid.* **B206**, 61 (1982); CALKUL Collaboration, F. A. Berends *et al.*, *ibid.* **B239**, 382 (1984); K. Hagiwara and D. Zeppenfeld, *ibid.* **B274**, 1 (1986); Z. Xu, D.-H. Zhang, and L. Chang, *ibid.* **B291**, 392 (1987); R. Gastmans and T. T. Wu, *The Ubiquitous Photon: Helicity Method for QED and QCD* (Oxford University Press, Oxford, 1990).

[20] G. 't Hooft and M. Veltman, Nucl. Phys. **B44**, 189 (1972).

[21] U. Baur, T. Han, and J. Ohnemus, Phys. Rev. D **48**, 5140 (1993).

[22] W. A. Bardeen, A. J. Buras, D. W. Duke, and T. Muta, Phys. Rev. D **18**, 3998 (1978).

[23] In Refs. [11,13 and 15] the factor $\lambda^{1/2}(\hat{s}, M_{V_1}^2, M_{V_2}^2)/(16\hat{s}^2)$, where $\lambda(a,b,c) = a^2 + b^2 + c^2 - 2(ab + ac + bc)$, was omitted from the virtual correction equations. Also in Ref. [13], the last term in the equation defining E_5 in the Appendix has the wrong sign; it should read $+8(U-T)/(S-4)$.

[24] LEP Collaborations, D. Decamp *et al.*, Phys. Lett. B **276**, 247 (1992).

[25] D. Schaile, Z. Phys. C **54**, 387 (1992).

[26] UA2 Collaboration, J. Alitti *et al.*, Phys. Lett. B **241**, 150 (1990); CDF Collaboration, F. Abe *et al.*, Phys. Rev. Lett. **65**, 2243 (1990); Phys. Rev. D **43**, 2070 (1991); H. Plothow-Besch, CERN Report No. CERN-PPE-90-168 (unpublished).

[27] A. D. Martin, R. G. Roberts, and W. J. Stirling, Phys. Lett. B **306**, 145 (1993).

[28] M. J. Duncan, G. L. Kane, and W. W. Repko, Phys. Rev. Lett. **55**, 773 (1985).

[29] V. Barger, A. D. Martin, and R. J. N. Phillips, Phys. Lett. **125B**, 339 (1983); E. L. Berger , D. DiBitonto, M. Jacob, and W. J. Stirling, *ibid.* **140B**, 259 (1984); H. Baer, V. Barger, H. Goldberg, and R. J. N. Phillips, Phys. Rev. D **37**, 3152 (1988).

[30] U. Baur, T. Han, and J. Ohnemus UC-Davis Report No. UCD-94-22 (unpublished).

[31] U. Baur, T. Han, and J. Ohnemus, UC-Davis Report No. UCD-94-5 (unpublished).

[32] K. O. Mikaelian, M. A. Samuel, and D. Sahdev, Phys. and D. Sahdev, Phys. Rev. D **20**, 1164 (1979); S. J. Brodsky and R. W. Brown, Phys. Rev. Lett. **49**, 966 (1982); R. W. Brown, K. L. Kowalski, and S. J. Brodsky, Phys. Rev. D **28**, 624 (1983); R. W. Brown and K. L. Kowalski, *ibid.* **29**, 2100 (1984).

[33] J. Ohnemus, Phys. Rev. D **47**, 940 (1993).

[34] J. F. Owens and W. K. Tung, Annu. Rev. Nucl. Part. Sci. **42**, 291 (1992).